Journal of Fluids and Structures 94 (2020) 102895

Contents lists available at ScienceDirect

Journal of Fluids and Structures

journal homepage: www.elsevier.com/locate/jfs

Verification of DES for flow over rigidly and elastically-mounted circular cylinders in normal and yawed flow

Xingeng Wu[1], Mohammad Jafari[1], Partha Sarkar[2], Anupam Sharma [*,3]

Department of Aerospace Engineering, Iowa State University, Ames, IA, 50011, United States of America

ARTICLE INFO

Article history:
Received 26 February 2019
Received in revised form 30 October 2019
Accepted 23 January 2020
Available online xxxx

Keywords:
Detached eddy simulations
Independence principle
Vortex-induced vibrations

ABSTRACT

A computational approach based on a k-ω delayed detached eddy simulation model for predicting aerodynamic loads on a smooth circular cylinder is verified against experiments. Comparisons with experiments are performed for flow over a rigidly-mounted (static) cylinder and for an elastically-mounted rigid cylinder oscillating in the transverse direction due to vortex-induced vibration (VIV). For the static cases, measurement data from the literature is used to validate the predictions for normally-incident flow. New experiments are conducted as a part of this study for yawed flow, where the cylinder axis is inclined with respect to the inflow velocity at the desired yaw angle, $\beta = 30°$. Good agreement is observed between the predictions and measurements for mean and rms surface pressure. Three yawed flow cases ($\beta = 15°, 30°, \& 45°$) are simulated and the results are found to be independent of β (independence principle) when the flow speed normal to the cylinder axis is selected as the reference velocity scale.

Dynamic (VIV) simulations for an elastically-mounted rigid cylinder are performed by coupling the flow solver with a solid dynamics solver where the cylinder motion is modeled as a mass–spring–damper system. The simulations accurately predict the displacement amplitude and unsteady loading over a wide range of reduced velocity, including the region where "lock-in" (synchronization) occurs. VIV simulations are performed at two yaw angles, $\beta = 0°$ and 45° and the independence principle is found to be valid over the range of reduced velocities tested with a slightly higher discrepancy when the vortex shedding frequency is close to the natural frequency of the system.

1. Introduction

Inclined and horizontally- or vertically-spanned cylinder are used in various engineering applications: cable-stayed, suspension, and tied-arch bridges, power transmission lines, offshore risers, sub-sea pipelines etc. These cylinders are prone to large-amplitude flow-induced vibration, which can lead to catastrophic failure of the cylinders and the structures supported by them. The vibration mechanisms involve complex aeroelastic (motion-induced) interactions that depend on

* Corresponding author.
E-mail address: sharma@iastate.edu (A. Sharma).
1 PhD Student.
2 Professor.
3 Associate Professor.

https://doi.org/10.1016/j.jfluidstructs.2020.102895
0889-9746/

the spatial orientation, geometry, surface-characteristics, and dynamic properties of the cylinders. Davenport (1995) shows that large amplitude vibrations can lead to either catastrophic- or fatigue failure of the cylinders and/or of the adjoining structures, which poses a significant threat to the safety and serviceability of these systems.

Flow induced vibration can be classified into the following categories: Kármán vortex-induced vibration (VIV), rain-wind induced vibration (RWIV), wake-induced vibration, and dry- or iced-cable galloping. While VIV and RWIV occur at relatively low wind speeds (< 20 m/s), wake-induced vibration and dry-cable galloping occur at higher speeds. Simulation of any of these aeroelastic phenomena requires accurate computation of the aerodynamic loads acting on the cable. This paper presents a comprehensive verification of a high-fidelity flow simulation technique (detached eddy simulations or DES) for flow over rigidly and elastically-mounted rigid circular cylinders in normal and yawed flow. The yaw angle (β) is defined as the angle between the cylinder axis and a vector orthogonal to the flow velocity vector in the plane of the cylinder axis. Yawed flow is considered because RWIV and dry-cable galloping occur only when β is non-zero. The diameter-based Reynolds number (Re_D) in the simulations is 2×10^4. At this Re_D, the boundary layer is laminar when it separates and transitions to turbulence in the free shear layer. The results of this paper are presented in two parts - the first part deals with rigidly-mounted (tethered/static) cylinders and the second part addresses elastically-mounted cylinders.

In the first part of the paper, simulations of flow over a static cylinder are verified with measurements from the literature as well as new experiments that are performed for $\beta = 0°$ and 30° as a part of this study. Comparisons between the simulations and the measurements include mean and rms of surface pressure, mean wake velocity profile, and power spectra of lift and drag. The agreement with the measured data ranges from very good to acceptable. Simulations are performed for four values of β ($= 0°,\ 15°,\ 30°$, and 45°) and the validity of the *independence principle* (IP) is examined. According to IP, the aerodynamic loads scaled using the velocity component normal to the cylinder axis are independent of β (Zdravkovich, 2003). Prior research (see e.g., Franzini et al. (2009) and Zhao et al. (2009)) has suggested the validity of IP for β up to 45°. The results of yawed flow simulations confirm the validity of IP for the static configurations analyzed.

The second part of the paper deals with vortex-induced vibrations (VIV). VIV are self-excited oscillations caused by the unsteady lift generated on a cylinder as a result of the vortex shedding in its wake. VIV is a common occurrence in many engineering structures, e.g., transmission lines, stacks, bridges, and offshore platform supports. Of particular interest is the phenomenon of "lock-in" or "synchronization" which occurs when the vortex-shedding frequency gets locked in with the natural frequency of the system. High but finite-amplitude (limit-cycle) oscillations are observed in this resonance condition due to non-linearity in the system. These high-amplitude oscillations can cause significant damage to the structure. VIV has been investigated extensively in the past few decades due to its practical significance. Bearman (1984), Sarpkaya (2004), Williamson and Govardhan (2004), Païdoussis et al. (2010), and Naudascher and Rockwell (2012) present detailed reviews on this topic.

Investigations of VIV over the past several decades, have resulted in an improved understanding of the phenomenon. Until recently, most of these investigations considered relatively high mass-damping systems. "Mass-damping" refers to a combined parameter that is a product of two parameters — mass ratio and damping ratio of a flow-excited system (see e.g. Scruton (1955) and Vandiver (2012)). In the last two decades, VIV of low mass-damping systems has garnered considerable interest due to the applicability of the phenomenon in marine engineering, offshore structures, moored structures, risers in offshore oil drilling rigs, etc. Such low mass-damping systems have been largely investigated using experiments (e.g., Jain and Modarres-Sadeghi (2013) and Franzini et al. (2013)) and semi-analytical methods that model vortex shedding using the classical Van der Pol oscillator (e.g., Xu et al. (2008)).

Experiments of VIV in low mass-damping systems have been typically conducted in water channels with partially or fully-submerged cylinders. Such setup can suffer from finite-span effects due to different end conditions at the two ends — wall on one side and free surface on the other. These effects are distinctly observable in yawed flow measurements (see e.g., Franzini et al. (2013)) where the results are found to be dependent on the direction with respect to the flow the cylinder is yawed (i.e., $\beta = 45°$ versus $-45°$). Computer simulations do not suffer from end effects as periodic boundary conditions enable modeling an infinitely long cylinder, although periodicity can introduce artificial effects if spanwise coherence length is greater than the simulated span (Wu and Sharma, 2020).

Numerical computations of VIV of low mass-damping systems have been performed using the Reynolds Averaged Navier–Stokes (RANS) equations (e.g., Guilmineau and Queutey (2004)), large eddy simulations or LES (e.g., Al-Jamal and Dalton (2004)), and direct numerical simulations or DNS (e.g., Lucor et al. (2005), Evangelinos et al. (2000), and Dong and Karniadakis (2005)). While the DNS approach is attractive from the perspective of resolving the entire turbulence spectrum, it is only feasible for very low Re_D flows due to the associated computation cost. LES is more feasible at moderate Re_D while Detached Eddy Simulations (DES) can be used over a very large range of Re_D without making the computations prohibitively expensive. DES (Spalart et al., 1997) is a non-zonal, hybrid RANS-LES approach that uses RANS to simulate attached flow near solid surfaces and LES for separated (detached) flow. A RANS turbulence model is used to compute the eddy viscosity for the sub-grid scale (SGS) stresses in the corresponding LES. In this paper, the phenomenon of VIV is investigated with elastically-mounted rigid cylinder simulations using DES and the results are verified against measured data available in the literature. The VIV simulations are performed at multiple values of β ($= 0°$ and 45°) and the validity of the independence principle for VIV of low mass-damping systems is verified.

This paper presents a comprehensive verification of DES for predicting flow over stationary and oscillating cylinders under normal and yawed flow. The hybrid RANS-LES nature of DES allows computations at arbitrarily high Reynolds

numbers (Re) and hence opens the possibility of solving real-world flow-induced vibration problems such as dry cable galloping which occur at high Re ($> 300,000$, see Macdonald and Larose (2006)), at a reasonable computational cost. This paper benchmarks the accuracy of DES in predicting aerodynamic loads on tethered and elastically-mounted rigid cylinders with detailed comparisons against multiple experimental datasets.

2. Computational methodology

The flow is approximated to be incompressible since the flow Mach number is less than 0.2. Denoting spatially filtered quantities by overhead tilde ($\tilde{}$), the filtered incompressible flow equations with an eddy-viscosity turbulence model are

$$\begin{aligned} \frac{\partial \tilde{U}_i}{\partial x_i} &= 0, \text{ and} \\ \frac{\partial \tilde{U}_i}{\partial t} + \frac{\partial (\tilde{U}_j \tilde{U}_i)}{\partial x_j} &= -\frac{1}{\rho}\frac{\partial \tilde{p}}{\partial x_i} + \nu \frac{\partial^2 \tilde{U}_i}{\partial x_j^2} - \frac{\partial \tau_{ij}}{\partial x_j}, \end{aligned} \tag{1}$$

where $\tau_{ij} = \widetilde{U_i U_j} - \tilde{U}_i \tilde{U}_j = -2\,\nu_{SGS}\,\tilde{S}$ and $\tilde{S} = (\partial \tilde{U}_i/\partial x_j + \partial \tilde{U}_j/\partial x_i)/2$. In the above, SGS denotes a sub-grid scale quantity, τ_{ij}^{SGS} denotes the sub-grid scale stress tensor which is modeled as the product of the eddy viscosity, ν_{SGS} and the strain rate tensor S_{ij}; turbulence models of such type are referred to as eddy-viscosity models. In the original DES formulation (Spalart et al., 1997), the Spalart–Allmaras (SA) LES and SA-RANS models were used. We use the method developed by Yin et al. (2015), which is called k-ω delayed detached eddy simulation, or k-ω DDES. This method uses a k-ω turbulence closure model in the RANS zones, and the same model is used to calculate the eddy viscosity (ν_T) in the LES zones. The eddy viscosity in the k-ω DES can be defined as $\nu_T = l_{DDES}^2\,\omega$, where l_{DDES} is the DDES length scale. The LES branch of this k-ω DDES model uses a dynamic procedure to compute the DDES model constant C_{DES} based on the flow configuration and grid size. This dynamic procedure has been shown to improve the DES capability by correcting for modeled stress depletion and log-layer mismatch (Yin et al., 2015). Note however that these improvements (specific to DDES) have little bearing on the problem considered here. The model has been implemented in the open source CFD software OpenFOAM. All the simulation results in this paper are obtained using OpenFOAM. The numerical scheme uses second order backward difference for time integration and linear interpolation with central differencing for spatial discretization of the governing equations.

2.1. Solid body dynamics and coupling

Simulations of VIV are performed with the pimpleDyMFoam solver which uses the *sixDoFRigidBodyMotion* feature of OpenFOAM. Single degree of freedom (dof) motion of the cylinder is considered here with displacement permitted only in the $y-$direction (orthogonal to the freestream flow direction). At each time step, pimpleDyMFoam calculates the motion and updates the displacement of the cylinder by integrating Eq. (2) in time using the Crank–Nicolson method.

$$m\,\ddot{y} + c\,\dot{y} + k_s\,y = F_{fluid}, \tag{2}$$

where m is the mass of the rigid cylinder, $\ddot{y}$, $\dot{y}$, and y are the instantaneous acceleration, velocity and displacement of the cylinder, respectively, c is the damping of the system, k_s is the spring stiffness and F_{fluid} is the transverse (cross-stream) component of the fluid force acting on the cylinder surface.

In order to maintain the quality of the meshes inside the boundary layer in dynamic simulations, the mesh around the cylinder (up to 1 diameter from the cylinder axis) moves with the cylinder without deforming. The mesh away from the cylinder is deformed based on the position of the cylinder. The solver then updates the fluxes according to the motion and uses the PIMPLE method to solve the incompressible Navier–Stokes equations.

2.2. Computational grid and mesh sensitivity study

The outer boundary of the computational domain is circular with a radius of $25 \times D$, where D is the diameter of the cylinder. The cylinder is placed in the center of the domain and the span dimension is $L = 10 \times D$ for all the simulations presented here. Periodic boundary conditions are used in the span direction, while freestream condition is used on the outer radial boundary. The domain is discretized using a multi-block grid that has three blocks: (1) an O-grid is used to resolve the flow around the cylinder, (2) an H-grid to resolve the wake, and (3) a C-grid for the far field. In order to accurately capture the aerodynamic forces on the cylinder, the flow around the cylinder and in the near-wake region has to be resolved with high precision. A fine mesh is therefore applied in these regions. Fig. 1 shows a cross-sectional view of the full computational domain as well as a zoom-view to highlight the grid topology.

A mesh sensitivity study is performed for normally-incident flow. Table 1 provides a summary of the three meshes used for this study. These are labeled 'Mesh 1', 'Mesh 2', and 'Mesh 3'. Cell counts, Strouhal number (St), mean drag coefficient ($\overline{C}_d$), mean back pressure coefficient ($\overline{C}_{pb}$), and root mean squared lift coefficient ($C_{l,rms}$) are compared between the three grids in the table. The St, $\overline{C}_d$, and $\overline{C}_{pb}$ are very close for Mesh 2 and Mesh 3. Fig. 2 compares the predicted mean aerodynamic pressure coefficient, $\overline{C}_p = 2(\overline{p} - p_\infty)/(\rho V_\infty^2)$ and the rms of pressure coeff., $C_{p'rms}$ for the different grids. Mesh

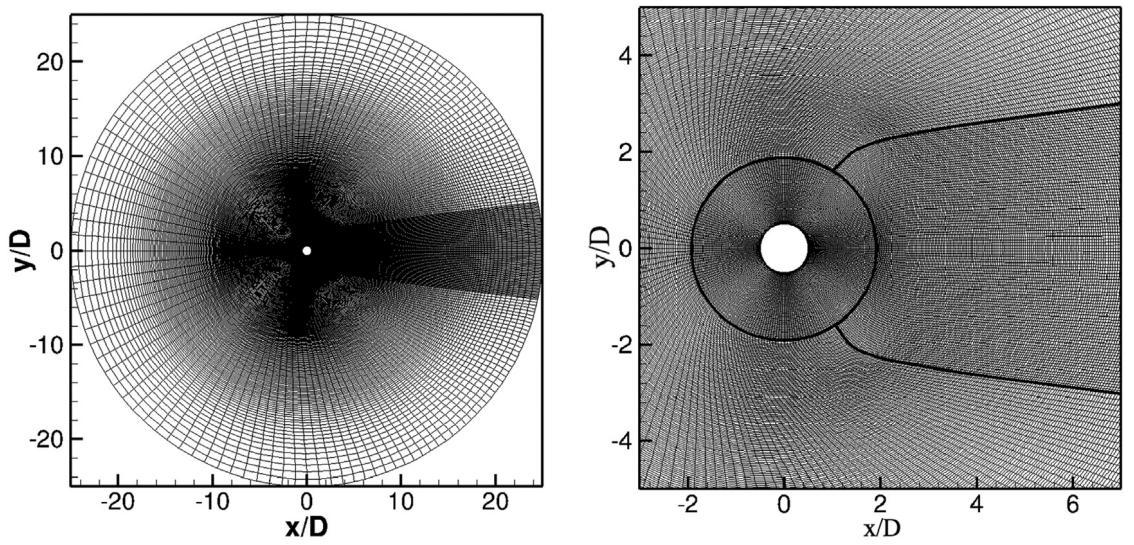

Fig. 1. Cross-sectional views of the computational grid.

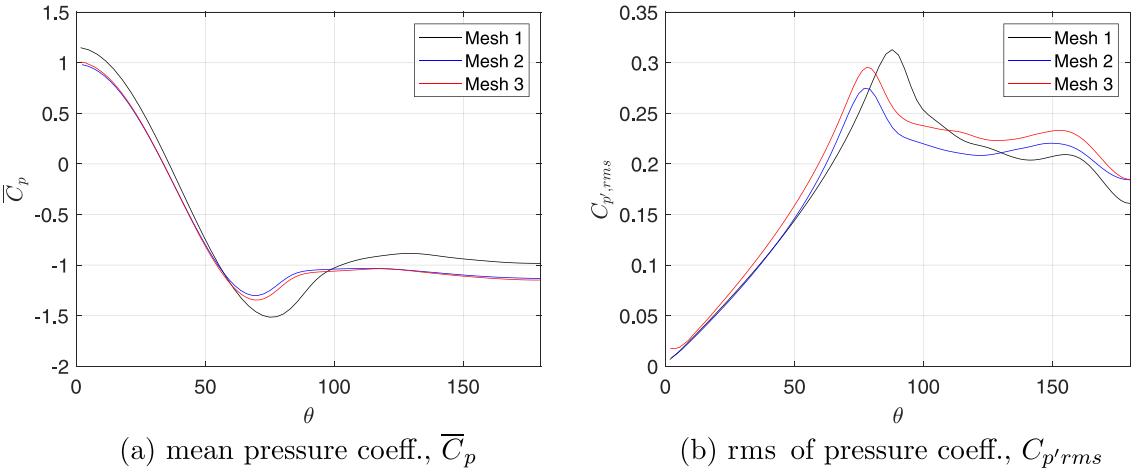

Fig. 2. Results of mesh refinement study.

Table 1
Summary of the test cases simulated to investigate sensitivity of results to mesh size. N_θ, N_r, and N_z denote number of cells in circumferential, radial, and span directions respectively. Also tabulated are St, $\overline{C}_d$, $\overline{C}_{pb}$ and $C_{l,rms}$.

Mesh	$N_\theta \times N_r \times N_z$	N_{total}	St	$\overline{C}_d$	$\overline{C}_{pb}$	$C_{l,rms}$
Mesh 1	157 × 233 × 65	2.37 M	0.201	1.065	−0.983	0.363
Mesh 2	188 × 275 × 80	4.14 M	0.208	1.125	−1.132	0.345
Mesh 3	236 × 343 × 100	8.09 M	0.208	1.137	−1.148	0.382

2 and Mesh 3 show consistent distributions of $\overline{C}_p$ and $C_{p'rms}$ and predict the same location for boundary layer separation ($\theta \sim 80°$); separation location is delayed with Mesh 1.

There is a modest difference in $C_{l,rms}$ in the static results (see Table 1). To assess the impact of this modest variation in $C_{l,rms}$ on the dynamic simulation results (presented in Section 5), one dynamic case is performed using Mesh 2 and Mesh 3. The peak scaled vibration amplitudes, $(A/D)_{max}$ are predicted to be 0.943 and 0.950 by Mesh 2 and Mesh 3. The difference is less than 0.75%, which demonstrates that the dynamic simulation results are also mesh independent. Mesh 3 is chosen for the subsequent static and dynamic simulations.

(a) setup for normal-flow measurements (b) setup for yawed flow measurements

Fig. 3. Pictures showing the model setup used to allow measurements at arbitrary inflow angles. The Cobra probe used to measure the wake is shown in (a).

3. Experimental setup and measurements

Static wind tunnel experiments were conducted on a smooth cylinder of circular cross section representing a stay cable to measure the aerodynamic forces and the velocity distribution in its wake. These experiments were performed in the Aerodynamic/Atmospheric Boundary Layer (AABL) Wind and Gust Tunnel located in the Department of Aerospace Engineering at Iowa State University. This wind tunnel has an aerodynamic test section of 2.44 m (8.0 ft) width × 1.83 m (6.0 ft) height and a design maximum wind speed of 53 m/s (173.9 ft/s). A polished aluminum tube with diameter, $D = 0.127$ m and length, $L = 1.52$ m was selected as the smooth cylinder model. Although the aspect ratio ($L/D = 12$) is sufficiently large to minimize edge effects at the mid-span of the circular cylinder, two circular plates of diameter $4D$ were attached to the ends of the cylinder. These plates were adjusted for each cylinder yaw angle to be parallel to the incoming airflow so that nearly 2D flow could be achieved over the cylinder. The maximum blockage ratio in the tunnel with the model was approximately 5% for all measurements. Fig. 3 displays the model setup in the AABL tunnel with the cylinder in normal-flow and yawed-flow configurations. An innovative multi-functional static setup was designed to measure the pressure distributions and velocity profiles for different yaw angles. As shown in Fig. 3, this setup properly secures the model for different yaw angles.

The model has 128 pressure taps distributed on its surface to measure local instantaneous pressure (see Fig. 5). These pressure values are used to compute aerodynamic lift and drag (viscous part ignored) on the cylinder as well as pressure correlations along the span. There are 36 pressure taps at equal angular spacing of 10 degrees along each of the three rings located on the cylinder. The three rings are labeled Right (R), Middle (M), and Left (L) as seen in Fig. 5(a) and are spaced $4D$ and $5D$ apart from each other along the span. Another set of pressure taps are located at a fixed angular location at equal spacing of $1D$ along the span between the rings (see Fig. 5 (a,b)).

A slight angular misalignment between the pressure probes and the inflow velocity vector can occur due to the rotation of the cylinder when it is mounted (see Fig. 4). The misalignment angle ζ is determined by requiring the mean lift coefficient, $\bar{C}_l$ to be zero for the static cases. Using this procedure, ζ is found to be 4.2° for the normal flow case and 0.57° for yawed flow ($\beta = 30°$). The experimental results (Exp-ISU) for $C_l^{(exp)}$ and $C_d^{(exp)}$ have been corrected as follows for the comparisons presented in this paper.

$$\begin{aligned} C_l^{\text{exp}} &= C_y = C_{y'} \cos\zeta + C_{x'} \sin\zeta \sim C_{y'} + C_{x'}\zeta \\ C_d^{\text{exp}} &= C_x = C_{x'} \cos\zeta - C_{x'} \sin\zeta \sim C_{x'} - C_{y'}\zeta \end{aligned} \tag{3}$$

3.1. Data acquisition system

For wake measurement, one Cobra Probe (4-hole velocity probe, TFI®.) mounted on a traverse system was used to measure the velocity field behind the model (see Fig. 3(a)). In order to minimize the blockage effect of the traverse system, its cross section was streamlined by using an airfoil section. For velocity measurements, the sampling rate was 1250 Hz and the sampling time was 60 s. Wake measurements were made $2.5D$ downstream of the model (measured from the cylinder axis), where the turbulence intensity was lower than the maximum allowable value (overall 30%) for the Cobra Probe.

Two 64-channel pressure modules (Scanivalve® ZOC 33/64 Px) were utilized to capture the local pressure. In addition, an Ethernet remote A/D system (ERAD) was used as a collection system to read information from the ZOC. The sampling rate and sampling time for all pressure measurements were 250 Hz and 60 s respectively. The Scantel program from

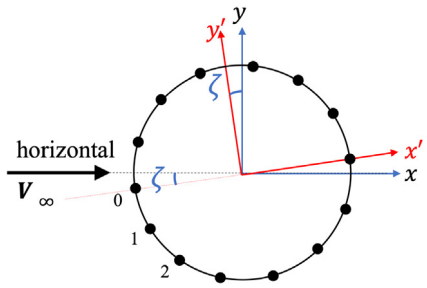

Fig. 4. Schematic illustrating misalignment of probe locations w.r.t. the inflow velocity ($\boldsymbol{V}_\infty$) due to cylinder rotation.

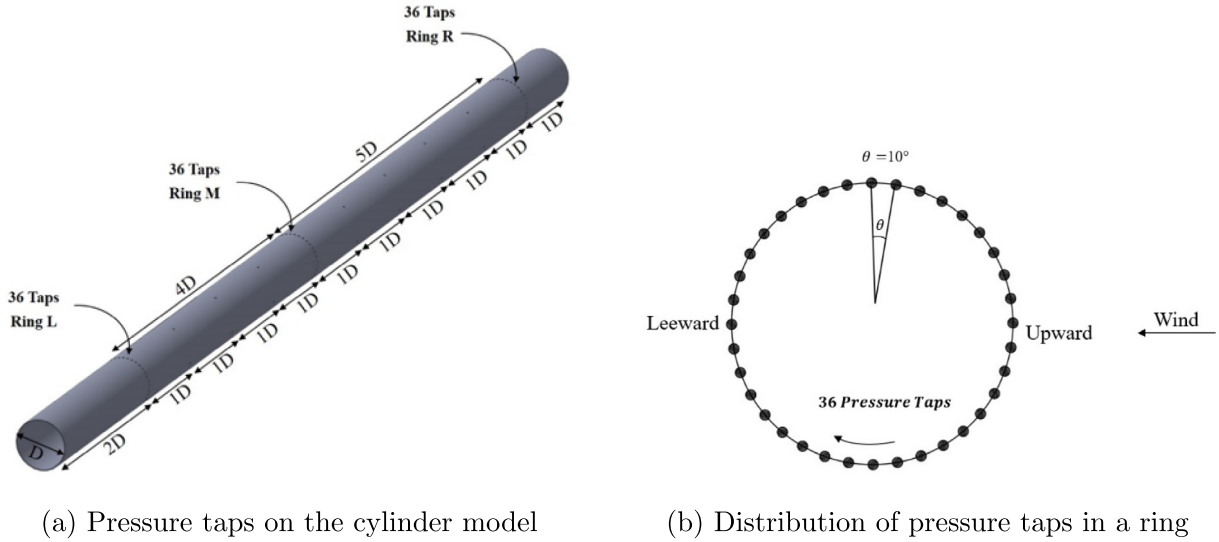

(a) Pressure taps on the cylinder model (b) Distribution of pressure taps in a ring

Fig. 5. Schematics illustrating the locations of surface pressure taps on the cylinder model.

Scanivalve was used for pressure data acquisition. In order to minimize the error of measurement due to the tube length, both ZOCs were placed inside the wind tunnel near the model (Fig. 3(b)). The wake measurement traverse system was removed when surface pressure measurements were made.

3.2. Measurement uncertainty

There are two major sources of error or uncertainty in any experimental study. The error from the first source depends on the precision of the instruments used in the experiment and is quantifiable. The second is the systematic and random error that originates from the experimental setup and environmental conditions, and hence is difficult to assess. The second error was minimized here by averaging over multiple (three) data runs. The error from the instruments in each of the measured parameters, aerodynamic pressure and force coefficients and normalized mean wind speed in the wake of the cylinder, can be estimated from the precision of the instruments that were used in this study. The precision of the pressure scanner (Scanivalve® ZOC 33/64) is 0.08% of the measured pressure, and the accuracy of the anemometer (TFI® Cobra probe) is 0.3 m/s (assuming a full range of 100 m/s) and a linear frequency-response from 0 to 2000 Hz. Based on this precision, the maximum error in the mean pressure coefficient ($\bar{C}_p$) is estimated to be $\pm 0.68\%$, whereas the maximum error in the rms pressure coefficient ($C_{p'rms}$) is estimated to be as high as $\pm 32\%$, which occurs in the separated flow region of the cylinder. The maximum error in the normalized velocities (u/V_∞), as measured in the wake of the cylinder, is estimated to be $\pm 0.6\%$.

4. Static-cylinder results

The objective of this paper is to demonstrate the capability of DES to predict aerodynamic loads on a static (tethered) cylinder and an elastically-mounted cylinder in normal and yawed flow. This section discusses the results of the simulations of flow over a static cylinder.

Table 2
Summary of results for normally-incident flow simulations.

Re_D	Method	St	$\overline{C}_d$	$\overline{C}_{pb}$
20,000	k-ω DDES	0.208	1.137	−1.148
20,000	Exp-I	0.194	1.156	−1.149
51,500	Exp-ISU	0.204	1.221	−1.305

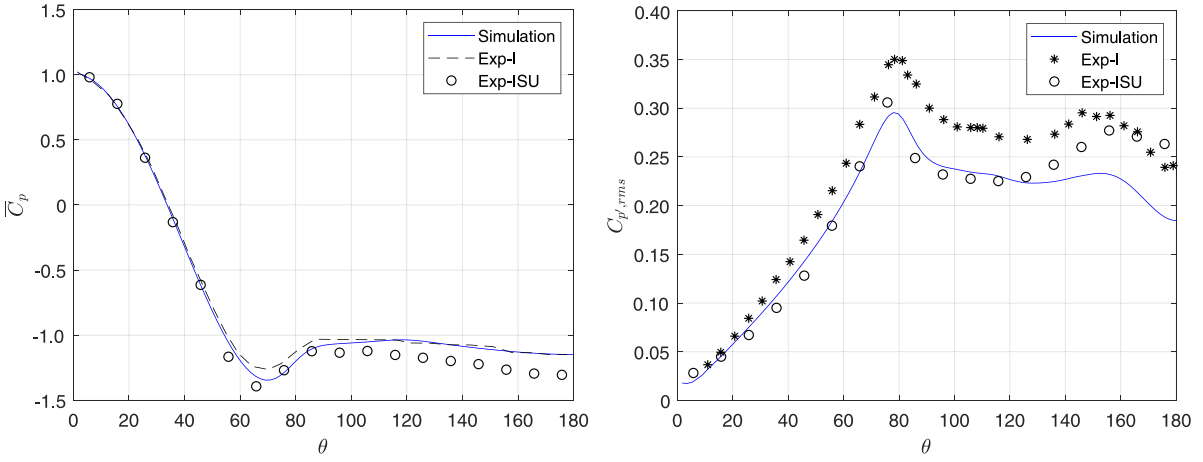

(a) mean pressure coeff., $\overline{C}_p$ (b) rms of pressure coeff., $C_{p'rms}$

Fig. 6. Comparisons of mean and rms of aerodynamic pressure coefficient between the simulation and experimental measurements.

Simulations are performed for (a) flow normal to the cylinder axis, and (b) flow at an angle to the cylinder axis (inclined/yawed cylinder); three yaw angles (β) are analyzed in this study. Smooth inflow is used — zero turbulence in the numerical simulations and the minimum possible inflow turbulence intensity (∼0.2%) in the tunnel. Cylinder surface is very smooth and hence surface roughness is not modeled in the simulations. Verification is performed with experimental data available in the literature, as well as data from the new experiments conducted as a part of this study.

4.1. Normally-incident flow

Table 2 summarizes the simulation results for the static cases and compares them with two sets of experimental data. Exp-I refers to the data from Norberg (2013) and Exp-ISU is from our measurements. Simulations are performed at $Re_D = 20{,}000$, which is the same as Exp-I, but the Re_D in Exp-ISU is higher ($= 51{,}500$). The Strouhal number (St), the mean drag coefficient, $\overline{C}_d$ and the mean back pressure coefficient, $\overline{C}_{pb}$ are compared in the table. Strouhal number is defined as $St = f_v D/V_\infty$, where f_v is the vortex-shedding frequency, D is the cylinder diameter, and V_∞ is the freestream flow speed.

Fig. 6 compares the predicted mean aerodynamic pressure coefficient, $\overline{C}_p$ and the root mean square of perturbation pressure coefficient, $C_{p'rms} = (\overline{C_p^2} - \overline{C}_p^2)^{1/2}$ with the data from the two experiments. The predicted $\overline{C}_p$ agrees very well with the data from Exp-I; Exp-ISU data shows slightly lower $\overline{C}_p$ than observed in Exp-I and the simulation, after 100°, and the mean back pressure, $\overline{C}_{pb}$ is lower as well. The predicted $C_{p'rms}$ distribution agrees well with the Exp-ISU data but is slightly lower than Exp-I. Both measurements as well as the simulation show the peak of $C_{p'rms}$ to be around 80°, which indicates the location of flow separation. The predicted distribution over the cylinder surface agrees well with the measurements.

Fig. 7 plots the predicted and measured wake velocity profiles at the axial station, $x/D = 2$; the cylinder axis is located at $x/D = 0$. The peak wake deficit and the wake profile are predicted accurately. The measured data shows a slight asymmetry in the data, which is perhaps due to the asymmetry in the experimental setup; the model is placed closer to the lower wall of the tunnel. The simulation data is averaged over 120 wake shedding cycles and the experimental data is averaged over 540 cycles.

Fig. 8 plots the predicted temporal variation of sectional lift and drag coefficients (C_l and C_d). As expected for a circular cylinder, the mean lift coefficient ($\overline{C}_l$) is zero but the mean drag coefficient ($\overline{C}_d$) is finite. The high-frequency oscillations which are apparent in the time history of C_l, are due to Kármán vortex shedding. The Strouhal number (St) is ∼ 0.2 as expected for bluff bodies for the Re_D considered here (see Travin et al. (2000) and Norberg (2013)). In addition to the oscillations at the vortex-shedding frequency (f_v), the entire signal appears to modulate at a frequency which is an order

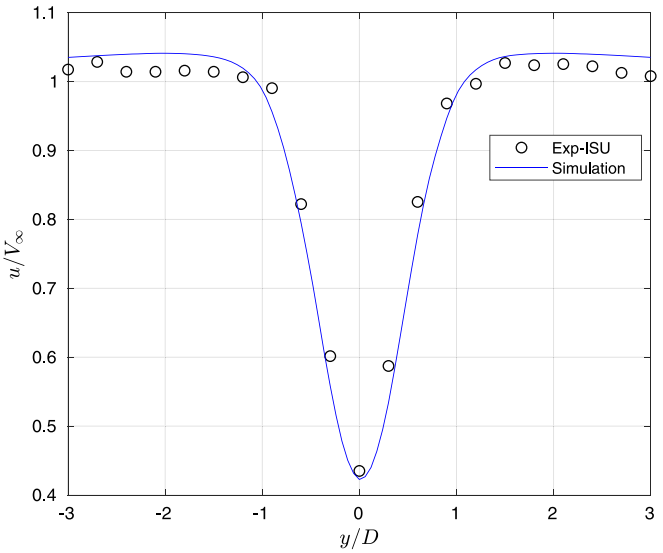

Fig. 7. Comparison of predicted and measured velocity profiles in the cylinder wake $2D$ downstream of the cylinder axis. u is the streamwise component of velocity and y is normal to the flow direction and the cylinder span.

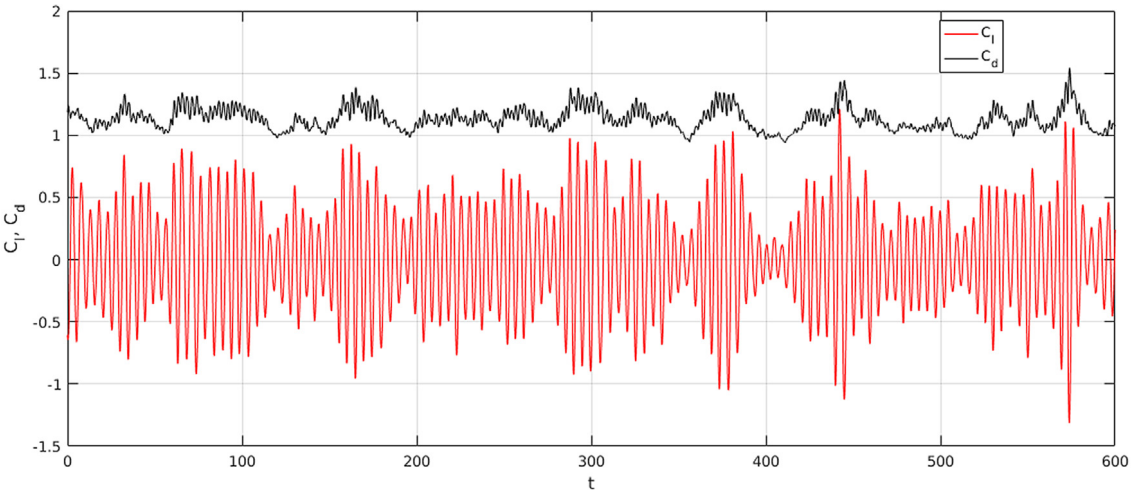

Fig. 8. Predicted temporal variations of lift and drag coefficients.

of magnitude lower than f_v. This modulation has a certain randomness to it and is not perfectly periodic. This modulation phenomenon has been reported elsewhere (Travin et al., 2000).

Fig. 9(a) compares the power spectral densities of C_l between the data from Exp-ISU and the simulation. Non-dimensional frequency, $k = fD/V_\infty$ is used to plot the spectra. The lift in the measurements is obtained by integrating the surface pressure measured using the pressure taps. Fig. 9(b) compares the PSD of C_d between the DES prediction and measurements. Because vortex shedding alternates between the top and bottom sides of the cylinder, one vortex shedding period contains two cycles of drag but only one cycle of lift. This can be seen in Fig. 9, where the spectral peak for C_l occurs at f_v while the spectral peak for drag is at $2f_v$. The agreement with the data is reasonable and the peak PSD for lift occurs around f_v corresponding to $k = St \sim 0.2$.

The peak frequency and its first three harmonics that occur at $k = 0.4, 0.6, \& 0.8$, are identified in the figure using vertical grid lines and labeled as $2f_v$, $3f_v$, $\& 4f_v$. The prediction and experiment both show a second, smaller peak in the lift spectrum at the third harmonic ($k = 0.6$). Since the lift vector alternates with the side the vortex sheds from, only odd harmonics of f_v (i.e., $3f_v$, $5f_v, \ldots$) are expected in the spectra. Therefore, no peak is observed in the lift spectra at the second harmonic ($k = 0.4$) or higher *even* harmonics in either the measured or the simulated data.

The overall spectral shapes of the PSDs of C_l and C_d are correctly predicted. However, the predicted PSD magnitudes at f_v and its harmonics are slightly higher and the broadband levels are slightly lower than the measured data. The reason

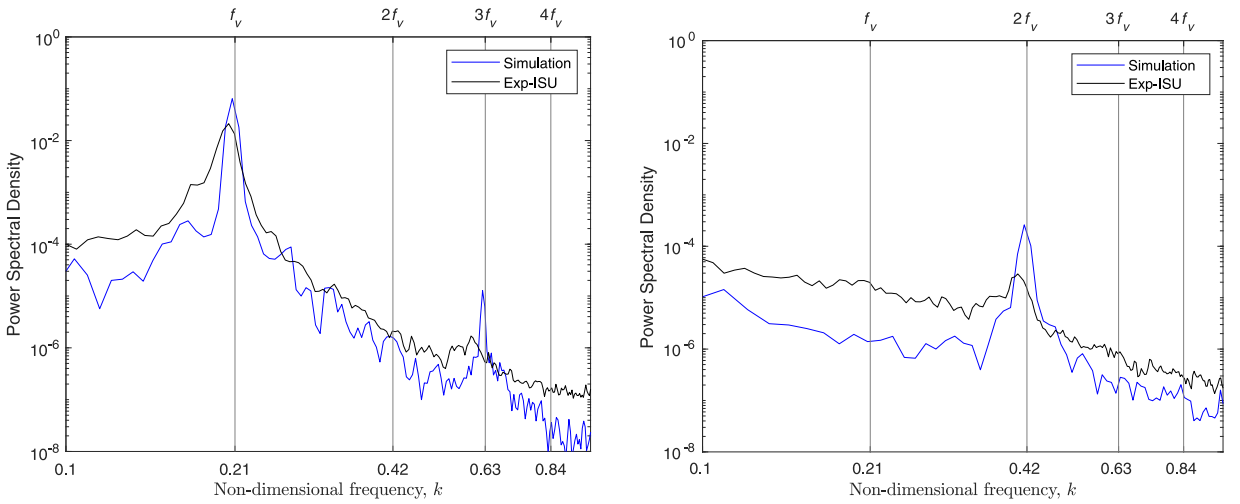

Fig. 9. Comparison of predicted and measured power spectral densities (PSDs) of C_l and C_d. The measured data is from our experiments (Exp-ISU).

for this disagreement is the ideal environment in the simulations which allows the vortex shedding to occur in a much tighter band of frequency (closer to a pure tone) than in the experiment. The experiments are performed in a non-ideal environment with inflow turbulence, tunnel blockage, potential vibration/motion of the cylinder due to flexibility, etc. This non-uniformity can lead to a generally higher broadband level in the measured spectra and "haystacking" around the tones — energy spreading into several frequency bins around the tones.

4.2. Yawed flow (inclined cylinder)

The schematic in Fig. 10 illustrates the setup for the inclined-cylinder simulations. The relative inclination of the cylinder axis with respect to the flow is obtained by yawing the flow rather than inclining the cylinder; these simulations are therefore also referred to as yawed-flow simulations. Other than yawing the inflow, the setup is exactly the same as for normally-incident flow.

The yaw angle, β is defined as the angle between the inflow velocity vector $\boldsymbol{V}_\infty$ and the x axis; the cylinder is aligned with the z axis (see Fig. 10). The normal component of the flow velocity is $V_n = V_\infty \cos\,\beta$ and the spanwise component is $V_z = V_\infty \sin\,\beta$, where $V_\infty = |\boldsymbol{V}_\infty|$. The computational domain is $L = 10 \times D$ long in the spanwise direction to investigate spanwise variation of aerodynamic forces.

Table 3 summarizes the Strouhal number (St) and the back pressure coefficient ($\overline{C}_{pb}$) for four different flow yaw angles, $\beta = 0, 15, 30, \& 45$ degrees. The velocity component normal to the cylinder axis (V_n) is used as the reference velocity scale to define a new set of non-dimensional quantities, such as Reynolds number, $Re_{D,n} = \rho V_n D/\mu$, Strouhal number, $St_n = f_v\, D/V_n$, and aerodynamic pressure coefficient, $\overline{C}_{p,n} = 2(\overline{p} - p_\infty)/(\rho V_n^2)$. The mean back pressure coefficient normalized in this manner is labeled as $\overline{C}_{pb,n}$. The measured value of $\overline{C}_{pb,n}$ is lower than that predicted by the simulations (see Table 3).

Fig. 11 compares with measured data the predicted mean aerodynamic pressure coefficient ($\overline{C}_{p,n}$) and the rms of perturbation pressure coefficient ($C_{p'rms,n}$), for $\beta = 30°$. The predicted back pressure ($\overline{C}_{pb,n}$) is found to be slightly higher than the Exp-ISU data, which is consistent with the observation for the normally-incident flow case. The predicted $C_{p'rms,n}$ distribution agrees very well with measurement, especially for $\theta < 120°$, where θ is the angular position on the cylinder surface measured from upstream. The peak of $C_{p'rms,n}$ is observed around 80° in both experiment and simulation, which is indicative of the location of separation of the shear layer.

Fig. 12(a) compares the predicted mean aerodynamic pressure coefficient ($\overline{C}_{p,n}$), for four different values of inflow yaw angle, β. The distribution of $\overline{C}_{p,n}$ is found to be very similar irrespective of β; Zdravkovich (2003) refers to this as 'independence principle' (IP). IP is also observed in the power spectral densities of the transverse force coefficient, $C_{y,n}$ for the same set of values of β analyzed. $C_{y,n} = 2f_y/(\rho V_n^2)$, where f_y is force per unit projected area ($f_y = F_y/(LD)$) in the y direction, and $C_{x,n}$ is correspondingly defined for the $x-$component of force. Fig. 12(b) shows that the spectra collapse when V_n is used to normalize the force coefficients and the frequency; the abscissa in Fig. 12(b) is $k_n = fD/V_n$.

Fig. 13 shows spatio-temporal plots of the force coefficients $C_{x,n}$ and $C_{y,n}$. The contours show that $C_{x,n}$ and $C_{y,n}$ vary along the span, indicating that vortex shedding does not occur simultaneously along the entire span. A spatial drift from

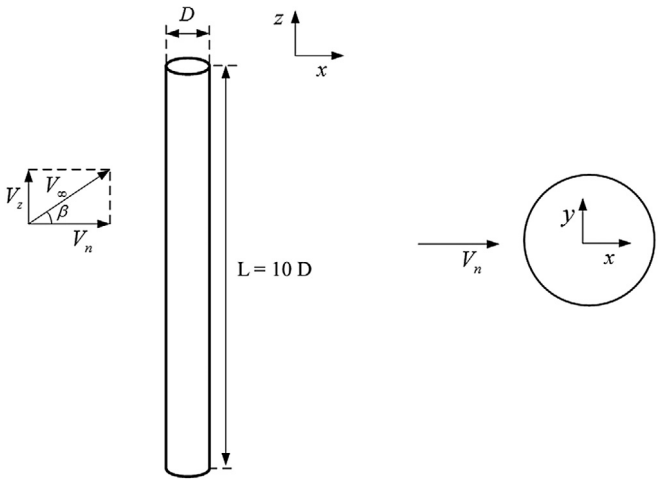

Fig. 10. A schematic of the computational setup for static inclined cylinder simulations. The right figure is a cross-sectional view. The inflow is set to an angle with respect to the cylinder axis, which stays aligned with the z axis of the coordinate system.

Table 3
Summary of simulation results for four different flow yaw angles ($\beta = 0, 15, 30,$ & 45 deg). Experimental data is only shown for $\beta = 30°$.

Method	flow angle, β	Re_D	$Re_{D,n}$	St_n	$\overline{C}_{pb,n}$
Simulation	0°	20,000	20,000	0.208	-1.148
Simulation	15°	20,000	19,318	0.202	-1.116
Simulation	30°	20,000	17,320	0.197	-1.108
Exp-ISU	30°	51,500	44,600	0.204	-1.073
Simulation	45°	20,000	14,142	0.207	-1.184

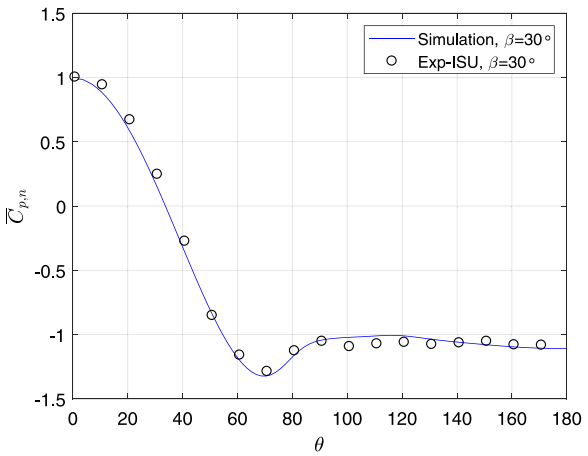

(a) mean pressure coeff., $\overline{C}_{p,n}$

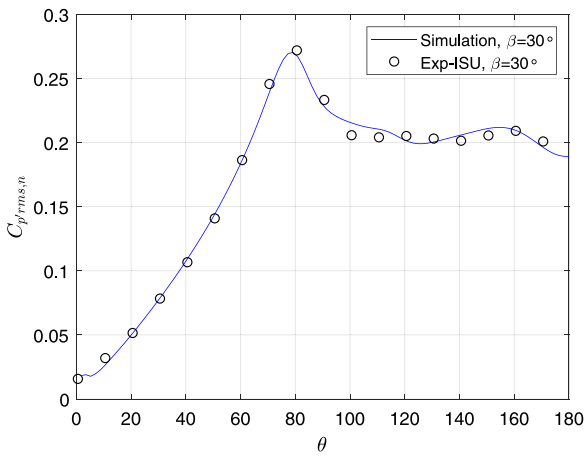

(b) rms of perturbation pressure, $C_{p'rms,n}$

Fig. 11. Comparisons between simulation and experimental measurements for $\beta = 30°$ yawed-flow case.

left to right with increasing time can be seen in the contours (more visible in the $C_{x,n}$ spatio-temporal plot) which is indicative of spanwise flow over the cylinder.

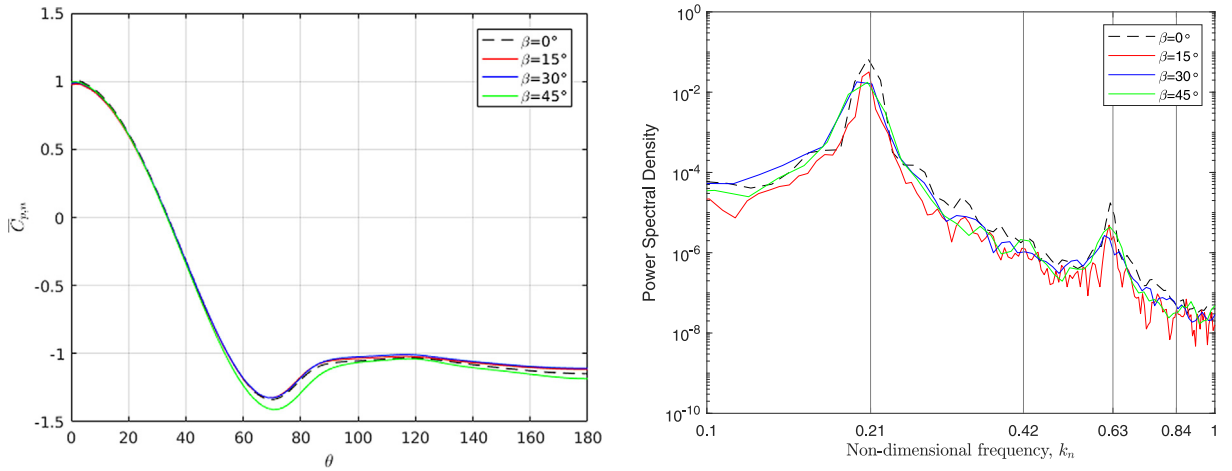

Fig. 12. Independence principle: comparisons of (a) $\overline{C}_{p,n}$, and (b) power spectral densities (PSDs) of $C_{y,n}$ between predictions for various β values.

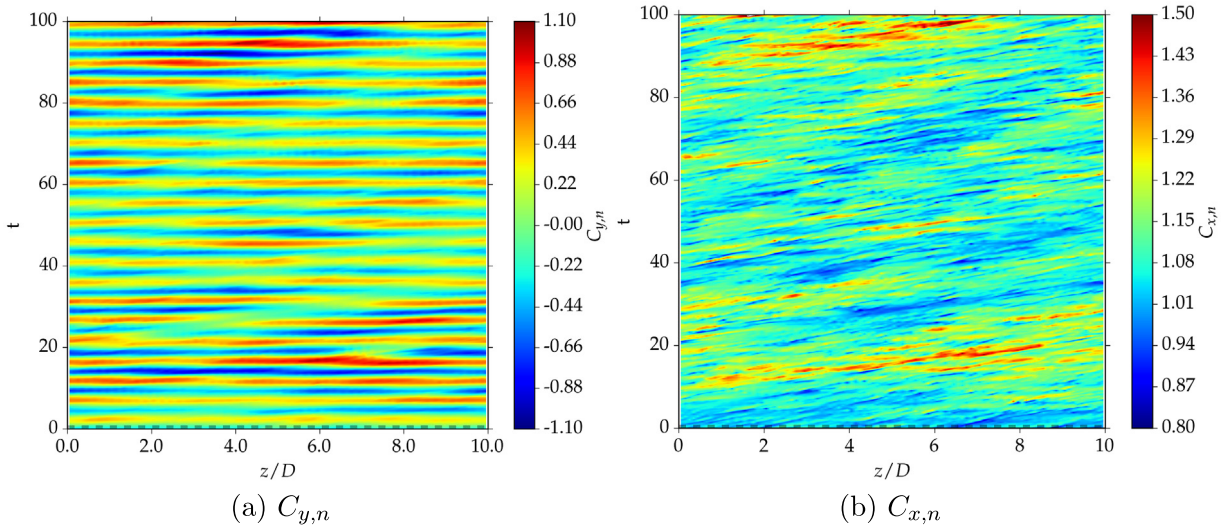

Fig. 13. Spatio-temporal distribution of force coefficients at $\beta = 30°$.

Fig. 14 presents coherence of force coefficients for $\beta = 30°$ case. Magnitude squared coherence, $\gamma^2(\Delta z)$ is defined as

$$\gamma^2(\Delta z) = \frac{\langle |S_{xy}|^2 \rangle}{\langle S_{xx} \rangle \langle S_{yy} \rangle}, \tag{4}$$

where S_{xy} denotes cross-spectral density of the quantity ($C_{x,n}$ or $C_{y,n}$) at two points separated by a distance Δz along the span, and S_{xx}, S_{yy} are auto-spectral densities; angular brackets denote ensemble averaging, however ergodicity assumption is used to relate that to time averaging. The coherence plot of $C_{y,n}$ indicates that spanwise correlation is very high (over nearly the entire cylinder span) at the vortex shedding frequency, but is small at other frequencies, which is expected based on literature. $C_{x,n}$ however is not that highly correlated along the span even at the peak vortex shedding frequency.

5. Vortex-induced vibration results

A schematic of the computational setup for vortex-induced vibration (VIV) simulations is presented in Fig. 15. The setup is the same as for the static simulations except for an additional mass–spring–damper system that determines the motion of the cylinder. The cylinder is constrained to move only in the cross-stream (y) direction. The y-component of the integrated aerodynamic surface force on the cylinder drives the mass–spring–damper system given by Eq. (2). Simulations are performed for eight inflow reduced velocities and two values of yaw angle, β (= 0° and 45°).

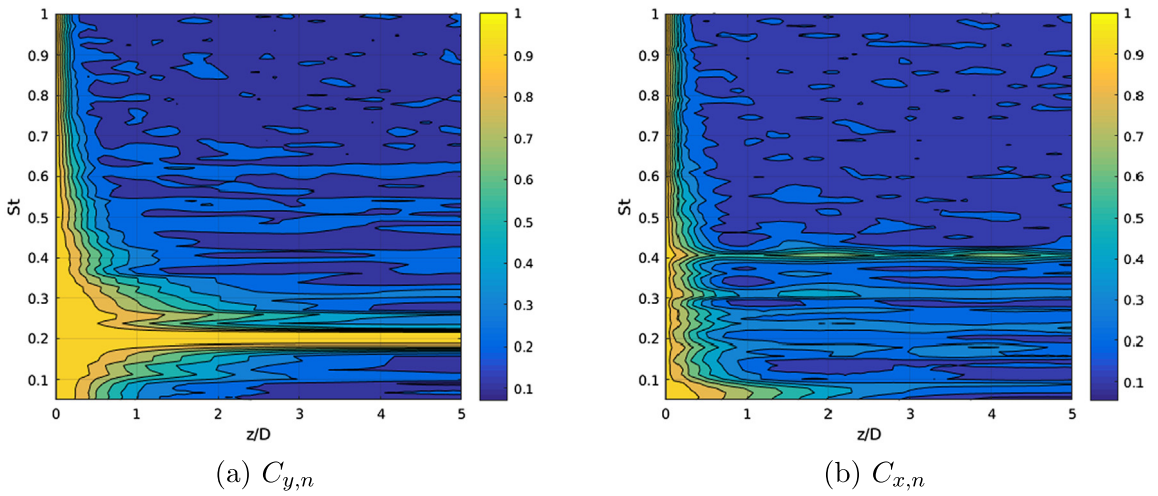

Fig. 14. Magnitude squared coherence, $\gamma^2(\Delta z)$ of transverse and longitudinal force coefficients - $C_{y,n}$ and $C_{x,n}$ for $\beta = 30°$ case.

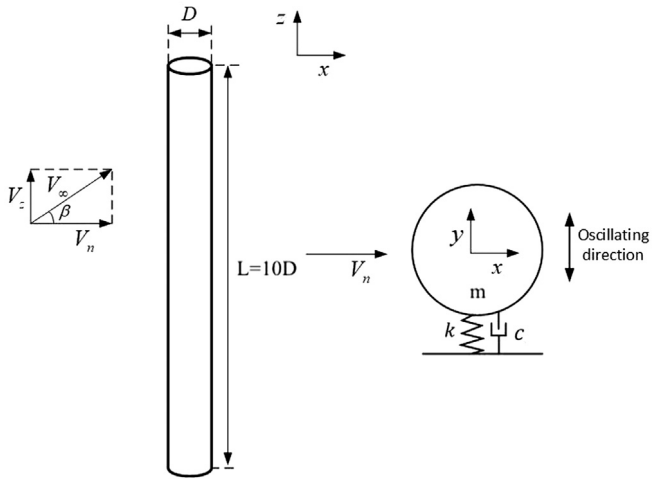

Fig. 15. A schematic of the computational setup for oscillating cylinder simulations. The right figure shows a cross-sectional view. The inflow is set to an angle with respect to the cylinder axis, which is aligned with the z-axis of the coordinate system.

In the simulations presented here, the mass ratio $m^* = m/(\rho\mathcal{V}) = 2.6$, where m is the mass of the cylinder, $\mathcal{V} = \pi(D^2/4)L$ is the volume of the cylinder, L is the cylinder span, and ρ is the density of the fluid flowing over the cylinder. The mechanical damping ratio of the system $\zeta_s = c/c_c$ is 0.001 where, $c_c = 2\sqrt{k_s.m}$ is the coefficient of critical damping, and k_s is the spring stiffness. The natural frequency of the system is $f_N = \sqrt{k_s/(m + m_a)}/(2\pi)$, where m_a is the 'added mass' of the fluid displaced by the cylinder. The added mass, $m_a = \rho\mathcal{V}C_A$, where C_A is the added mass coefficient which is typically taken to be 1.0 ± 0.05 for small transverse oscillations (Khalak and Williamson, 1997); C_A is assumed to be equal to 1 here.

To accommodate for yawed flow, the reduced velocity is defined as, $V_{R,n} = V_n/(f_N D)$, where the subscript n refers to the component of the velocity vector normal to the cylinder axis. Two different yaw angles are evaluated, $\beta = 0°$ and 45°, at $Re_D = 20{,}000$. The non-dimensional parameters, m^*, ζ_s, and $V_{R,n}$ are selected to match the measurements of Franzini et al. (2013). This measurement dataset is referred as Exp II in this paper. $V_{R,n}$ is varied in the experiments by changing the freestream flow speed, which changes Re_D. In the simulations, $V_{R,n}$ is varied by changing the spring stiffness, and Re_D is held constant. In addition to Exp II, the simulation results are also compared to another dataset reported in Khalak and Williamson (1997), which is referred as Exp III here. The values of m^* (= 2.4) and ζ_s (= 0.0045) in Exp III are slightly different from Exp II and the simulations.

Fig. 16 compares the predicted scaled mean displacement amplitude ($\bar{A}/D$) with the measurements of Exp II and III over a wide range of $V_{R,n}$. Khalak and Williamson (1997) identified the following four distinct branches in the $\bar{A}/D$ versus $V_{R,n}$ plot of their VIV measurements for the zero-yaw case: the "initial excitation" branch, the "upper" branch, the "lower"

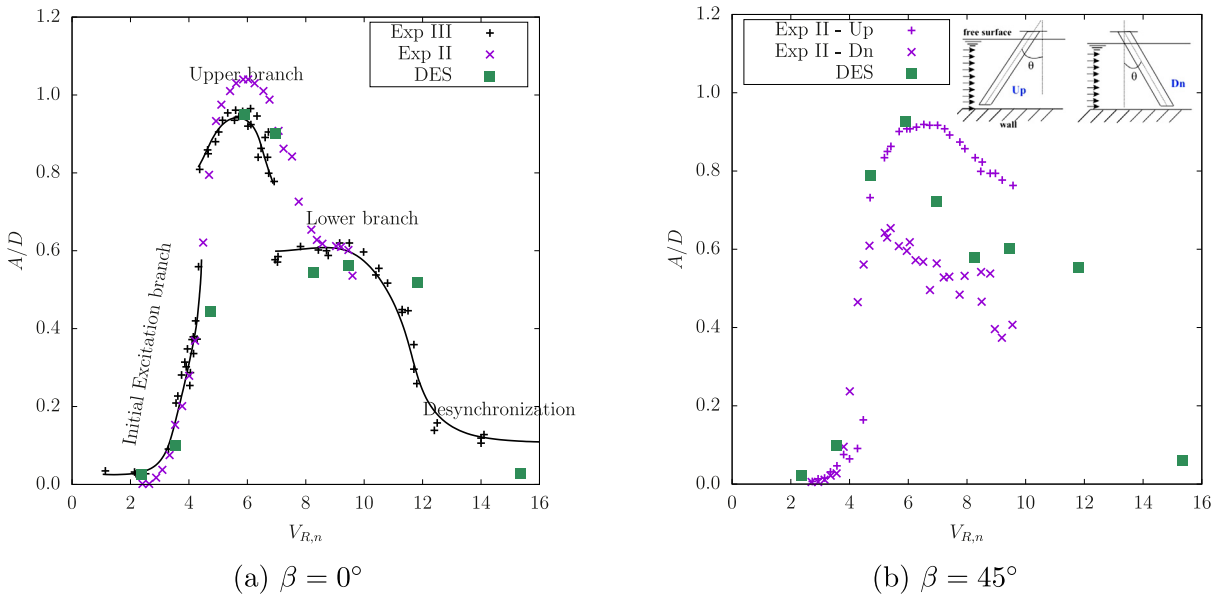

Fig. 16. Comparison of predicted and measured non-dimensional mean amplitude, $\bar{A}/D$ over a range of reduced velocities $V_{R,n}$ for (a) $\beta = 0°$, and (b) $\beta = 45°$. The inset in the plot on the right shows the two setups (UP and DN) used in Exp II for yawed-flow measurements.

branch, and the "desynchronization" branch. These are labeled and identified with solid black lines as best curve fits of the measured data in Fig. 16(a). Note that the variation of $\bar{A}/D$ with $V_{R,n}$ is topologically different for systems with high mass and damping, e.g., measurements of Feng (1968) show two branches (multi-valued solution) in the lock-in regime. For the selected low mass-damping system, $\bar{A}/D$ grows rapidly with $V_{R,n}$ in the *initial excitation* branch, reaches a peak in the *upper* branch, then reduces to 60% of the peak value in the *lower* branch, and finally drops to a negligible value at higher $V_{R,n}$ in the *desynchronization* branch. The current DES results agree very well with the data (particularly with Exp III) in the *initial excitation* and *upper* branches. The peak amplitude is well captured. The predicted amplitude is slightly lower than the measurements in the *lower* and *desynchronization* branches. Considering the relatively large differences in the two sets of measurements (Exp II and Exp III), which provides an estimate of uncertainty/repeatability, the prediction accuracy of the simulations is very good.

Fig. 16(b) compares the predicted VIV amplitude with the data from Exp II for $\beta = 45°$. The measurements were taken for two different configurations of the cylinder, which are shown in the inset in the figure. Since the top and bottom surfaces are not the same, the two configurations are not identical and the measured data for the two configurations shows a large difference. Since the setup in the experiment is asymmetric (wall at the bottom and free surface on the top) and the fact that end plates were not used, end effects (finite-span effect) might be the reason for the observed differences between the two configurations. The predictions agree better with the "Up" configuration in the *initial excitation* and *upper* branches, and with the "Dn" configuration in the *lower* branch. Exp II did not collect any data at higher $V_{R,n}$ to test the prediction accuracy in the *desynchronization* branch.

5.1. Modes of vortex shedding

As seen in Figs. 16 and 18, the amplitude jumps up from the *initial excitation* branch to the *upper* branch, and jumps down from the *upper* branch to the *lower* branch as $V_{R,n}$ is increased. These jumps occur as the mode in which the vortex shedding occurs switches between two possible configurations. These modes are illustrated in Fig. 17 using schematics and contours of the Q-criterion drawn on a cross-sectional plane at mid span. In the '2S' mode, two single vortices shed alternately from either side of the cylinder in one cycle of cylinder motion, while in the '2P' mode, two pairs of vortices are shed from each side of the cylinder in one cycle. The 2P mode has been observed in the smoke visualizations of Brika and Laneville (1993). In the *initial excitation* branch, vortex shedding occurs in the 2S mode, while in the *lower* branch, it switches to the 2P mode. In the *upper* branch of the lock-in regime, the vortex shedding switches between the 2S and 2P modes. Other modes of vortex shedding have also been observed (e.g., 2P+S and P+S modes) in forced vibration motion (see e.g., Williamson and Roshko (1988)).

5.2. Independence principle in VIV

This section investigates the validity of the *independence principle* on frequency and amplitude of displacement of an elastically-mounted rigid cylinder undergoing VIV. Prior experiments (e.g., Jain and Modarres-Sadeghi (2013) and Franzini

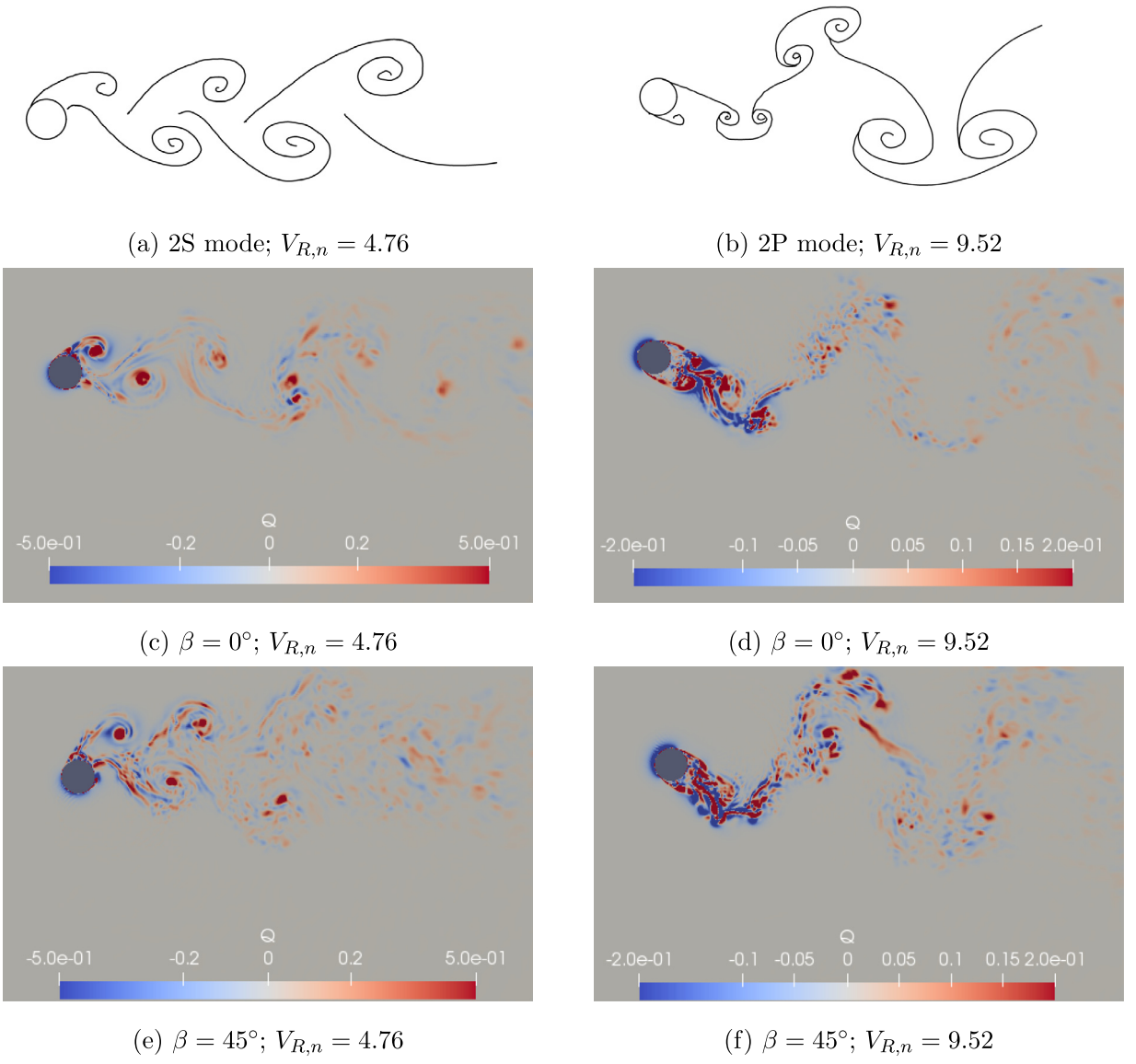

Fig. 17. Illustration of the two modes of vortex shedding observed in the simulations using schematics in (a) & (b), and contour plots of the Q-criterion at mid span for $\beta = 0°$ in (c) & (d) and $\beta = 45°$ in (e) & (f).

et al. (2013)) have investigated IP for a circular cylinder. Zhao (2015) and Bourguet et al. (2015) have numerically investigated IP using DNS but at very low Reynolds number ($Re_D < 1,000$). Much higher Re_D (= 20,000) is considered in this work and the current methodology (DES) can scale to significantly higher Re_D without a substantial increase in computation cost.

The data from Franzini et al. (2013) (Exp II) is plotted in Fig. 18(a) and the DES predictions in Fig. 18(b) for the two yaw angles evaluated ($\beta = 0°$ and 45°). The DES predictions show little difference between $\beta = 0°$ and 45° except around $V_{R,n} = 4.76$ and 7, where $\bar{A}/D$ is highly sensitive to changes in $V_{R,n}$. As far as the general variation of $\bar{A}/D$ with $V_{R,n}$ (identified by solid lines in Fig. 18(b)) is considered, the predictions for both yaw angles show the same behavior, suggesting that the independence principle also holds for VIV. From the measurements however, one can only conclude that IP holds primarily in the Initial Excitation branch. The large difference in the measurements between the Up and Dn configurations for $\beta = 45°$ limits the verification of IP in VIV to the *initial excitation* branch.

Fig. 19 compares the vortex shedding frequency normalized by the natural frequency of the system (f_v/f_N) between the DES predictions and the measurements from Exp III over a range of $V_{R,n}$. The purple dashed line corresponds to the peak vortex-shedding frequency for a static cylinder ($St \sim 0.2$) and the black dashed line corresponds to $f_v = f_N$. The simulations capture the variation of vortex-shedding frequency over the entire range of $V_{R,n}$ tested. In the *initial*

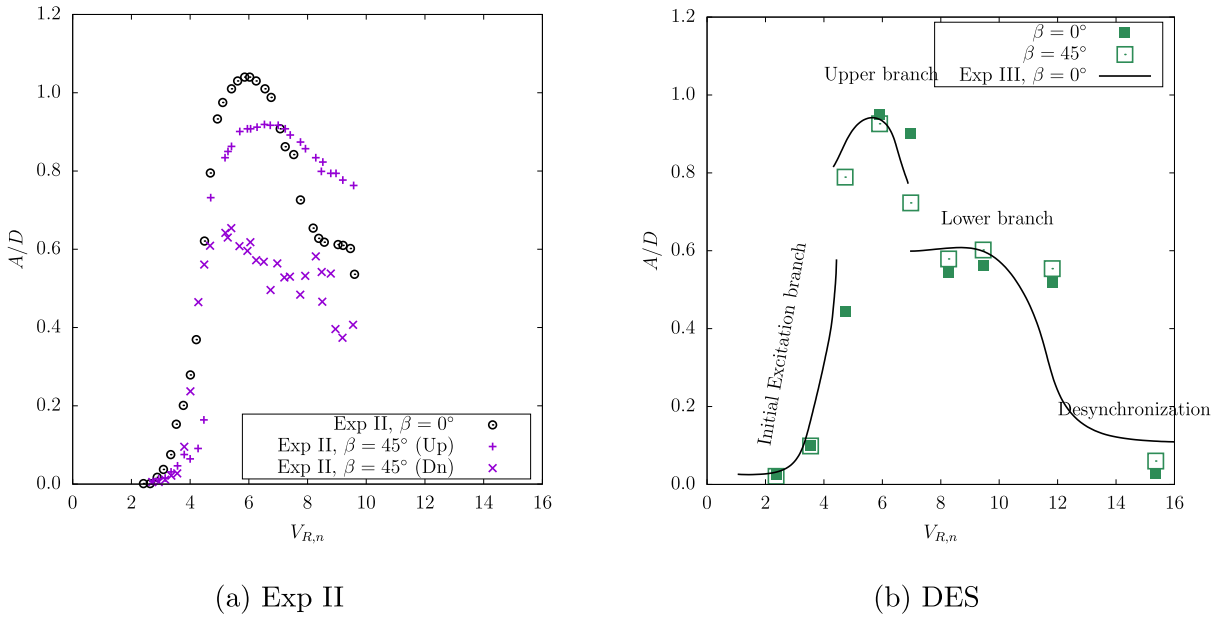

Fig. 18. Scaled mean displacement amplitude $\bar{A}/D$ for $\beta = 0°$ and 45° degrees for a range of $V_{R,n}$ obtained from (a) measurements from Exp II, and (b) DES predictions with the data from Exp III for $\beta = 0°$ as a guide.

excitation branch, f_v increases linearly with the reduced velocity $V_{R,n}$. Beyond resonance, which occurs around $f_v = f_N$, the vortex shedding frequency gets "locked-in" with the natural frequency of the system. This occurs in the *upper* and *lower* branches identified in Fig. 16(a). The added mass of the fluid causes the lock-in frequency to be higher than f_N, particularly for low-m^* systems. As $V_{R,n}$ increases beyond lock-in, the vortex shedding frequency desynchronizes with the natural frequency and f_v/f_N again follows the purple line in the figure. Fig. 19 also plots the simulation results for $\beta = 45°$, which are nearly coincident with the results for $\beta = 0°$, verifying IP.

It should be emphasized that the validity of the independence principle is determined here primarily from the peak amplitude and the lock-in frequency. Similar comparisons have been used elsewhere (e.g., Franzini et al. (2013), Zhao (2015)) to establish IP. It should also be noted that the conclusion of IP for VIV is limited to elastically-mounted *rigid* cylinders; Seyed-Aghazadeh and Modarres-Sadeghi (2018) have shown that the independence principle is not valid for flexible structures and the frequency response and the excited structural modes for yaw angles as small as 15° are different from the normal-flow case.

6. Conclusion

A computational methodology based on a k-ω delayed detached eddy simulation (DDES) model is used to investigate aerodynamic loading on a smooth circular cylinder. Simulations are performed for a static and an elastically-mounted rigid cylinder in normally-incident flow and yawed flow. For static-cylinder configuration, the computational methodology is verified against experimental data in normally-incident flow ($\beta = 0°$) and yawed flow ($\beta = 30°$). The agreement between the simulations and the experiments for normally-incident flow and yawed flow is good. These favorable comparisons demonstrate the ability of the DES methodology to accurately predict aerodynamic loading on static circular cylinders. Simulation results for different flow angles ($\beta = 0°$, 15°, 30°, & 45°) also verify the validity of the independence principle for β up to 45°.

For the elastically-mounted rigid cylinder (vortex-induced vibration) simulations, the dynamics of the cylinder is modeled using a forced mass–spring–damper system with a low mass ratio and low damping, and the cylinder is constrained to move only in the transverse direction. The simulation results are compared with two sets of existing experimental data and the agreement of the predicted displacement amplitude and vortex shedding frequency with the measurements is found to be good over a wide range of reduced velocity. The frequency lock-in phenomenon is captured by the simulations. Different modes of vortex shedding (2S and 2P) are observed in the simulations and are identified using contour plots of the Q-criterion at the mid-span location. Results for two values of β (= 0° and 45°) are compared and, barring some difference in the regions where the displacement amplitude is highly sensitive to the reduced velocity, the independence principle is found to hold for rigid circular cylinders in VIV up to a yaw angle of 45°.

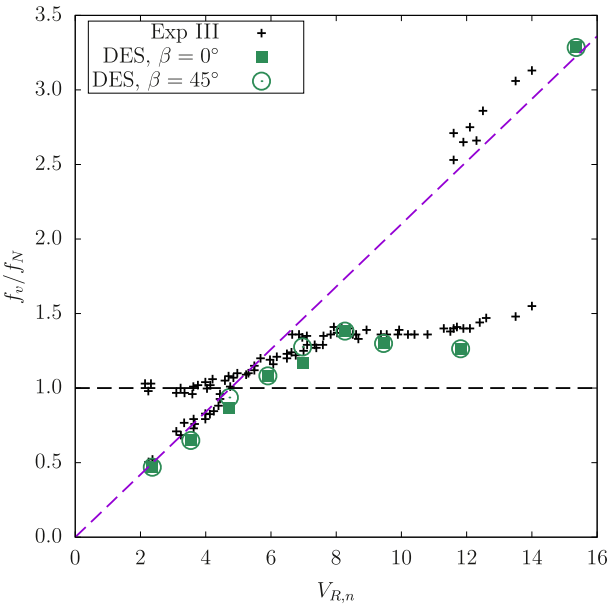

Fig. 19. Non-dimensional frequency f_v/f_N for various reduced velocities $V_{R,n}$.

Declaration of competing interest

The authors declare that they have no known competing financial interests or personal relationships that could have appeared to influence the work reported in this paper.

Acknowledgments

Funding for this research is provided by the National Science Foundation, United States of America (Grant #NSF/ CMMI-1537917). Computational resources are provided by NSF XSEDE, United States of America (Grant #TG-CTS130004) and the Argonne Leadership Computing Facility, which is a DOE Office of Science User Facility, United States of America supported under Contract DE-AC02-06CH11357.

References

Al-Jamal, H., Dalton, C., 2004. Vortex induced vibrations using large eddy simulation at a moderate reynolds number. J. Fluids Struct. 19 (1), 73–92.
Bearman, P.W., 1984. Vortex shedding from oscillating bluff bodies. Annu. Rev. Fluid Mech. 16 (1), 195–222.
Bourguet, R., Karniadakis, G.E., Triantafyllou, M.S., 2015. On the validity of the independence principle applied to the vortex-induced vibrations of a flexible cylinder inclined at 60°. J. Fluids Struct. 53, 58–69.
Brika, D., Laneville, A., 1993. Vortex-induced vibrations of a long flexible circular cylinder. J. Fluid Mech. 250, 481–508.
Davenport, A., 1995. The dynamics of cables in wind. In: Proceedings of Symposium on Cable Dynamics.
Dong, S., Karniadakis, G.E., 2005. DNS of flow past a stationary and oscillating cylinder at re = 10000. J. Fluids Struct. 20 (4), 519–531.
Evangelinos, C., Lucor, D., Karniadakis, G., 2000. DNS-derived force distribution on flexible cylinders subject to vortex-induced vibration. J. Fluids Struct. 14 (3), 429–440.
Feng, C., 1968. The Measurement of Vortex Induced Effects in Flow Past Stationary and Oscillating Circular and d-Section Cylinders (Ph.D. thesis). University of British Columbia.
Franzini, G., Fujarra, A.L.C., Meneghini, J.R., Korkischko, I., Franciss, R., 2009. Experimental investigation of vortex-induced vibration on rigid, smooth and inclined cylinders. J. Fluids Struct. 25 (4), 742–750.
Franzini, G.R., Gonçalves, R.T., Meneghini, J.R., Fujarra, A.L.C., 2013. One and two degrees-of-freedom vortex-induced vibration experiments with yawed cylinders. J. Fluids Struct. 42, 401–420.
Guilmineau, E., Queutey, P., 2004. Numerical simulation of vortex-induced vibration of a circular cylinder with low mass-damping in a turbulent flow. J. Fluids Struct. 19 (4), 449–466.
Jain, A., Modarres-Sadeghi, Y., 2013. Vortex-induced vibrations of a flexibly-mounted inclined cylinder. J. Fluids Struct. 43, 28–40.
Khalak, A., Williamson, C., 1997. Fluid forces and dynamics of a hydroelastic structure with very low mass and damping. J. Fluids Struct. 11 (8), 973–982.
Lucor, D., Foo, J., Karniadakis, G., 2005. Vortex mode selection of a rigid cylinder subject to viv at low mass-damping. J. Fluids Struct. 20 (4), 483–503.
Macdonald, J.H., Larose, G.L., 2006. A unified approach to aerodynamic damping and drag/lift instabilities, and its application to dry inclined cable galloping. J. Fluids Struct. 22 (2), 229–252.
Naudascher, E., Rockwell, D., 2012. Flow-Induced Vibrations: An Engineering Guide. Courier Corporation.
Norberg, C., 2013. Pressure forces on a circular cylinder in cross flow. In: Eckelmann, H., Graham, J.M.R., Hierre, P., Monkewitz, P.A. (Eds.), IUTAM Symposium on Bluff Body Wakes, Dynamics and Instabilities. pp. 275–278.

Païdoussis, M.P., Price, S.J., De Langre, E., 2010. Fluid–Structure Interactions: Cross-Flow-Induced Instabilities. Cambridge University Press.
Sarpkaya, T., 2004. A critical review of the intrinsic nature of vortex-induced vibrations. J. Fluids Struct. 19 (4), 389–447.
Scruton, C., 1955. Wind-excited oscillations of tall stacks. The Engineer 199 (5185), 806–808.
Seyed-Aghazadeh, B., Modarres-Sadeghi, Y., 2018. An experimental study to investigate the validity of the independence principle for vortex-induced vibration of a flexible cylinder over a range of angles of inclination. J. Fluids Struct. 78, 343–355.
Spalart, P., Jou, W., Strelets, M., Allmaras, S., et al., 1997. Comments on the feasibility of LES for wings and on a hybrid RANS/LES approach. Adv. DNS/LES 1, 4–8.
Travin, A., Shur, M., Strelets, M., Spalart, P., 2000. Detached-eddy simulations past a circular cylinder. Flow Turbul. Combust. 63 (1–4), 293–313.
Vandiver, J.K., 2012. Damping parameters for flow-induced vibration. J. Fluids Struct. 35, 105–119.
Williamson, C., Govardhan, R., 2004. Vortex-induced vibrations. Annu. Rev. Fluid Mech. 36, 413–455.
Williamson, C.H., Roshko, A., 1988. Vortex formation in the wake of an oscillating cylinder. J. Fluids Struct. 2 (4), 355–381.
Wu, X., Sharma, A., 2020. Artefacts of finite span in vortex-induced vibration simulations. J. Appl. Ocean. Res. under review.
Xu, W.-H., Zeng, X.-H., Wu, Y.-X., 2008. High aspect ratio (l/d) riser viv prediction using wake oscillator model. Ocean Eng. 35 (17–18), 1769–1774.
Yin, Z., Reddy, K., Durbin, P.A., 2015. On the dynamic computation of the model constant in delayed detached eddy simulation. Phys. Fluids 27 (2), 025105.
Zdravkovich, M.M., 2003. Flow Around Circular Cylinders: Volume 2: Applications, vol. 2, Oxford university press.
Zhao, M., 2015. The validity of the independence principle applied to the vortex-induced vibration of an inclined cylinder in steady flow. Appl. Ocean Res. 53, 155–160.
Zhao, M., Cheng, L., Zhou, T., 2009. Direct numerical simulation of three-dimensional flow past a yawed circular cylinder of infinite length. J. Fluids Struct. 25 (5), 831–847.